*Int. J. Electrochem. Sci.*, 8 **(2013)** 2345 - 2353

International Journal of
ELECTROCHEMICAL
SCIENCE
www.electrochemsci.org

# Facile Synthesis of Mesoporous $SnO_2$ Submicrospheres by Microemulsion Approach as High-Capacity Anodes Material for Lithium-Ion Batteries

*Hui-Yuan Wang, Guang-Yin Liu*[*], *Zhi-Zheng Yang, Bang-Yong Wang, Lei Chen, Qi-Chuan Jiang*[*]

Key Laboratory of Automobile Materials of Ministry of Education & School of Materials Science and Engineering, Jilin University, Changchun 130025, China
[*]E-mail: wanghuiyuan@jlu.edu.cn; liugy10@mails.jlu.edu.cn

*Received:* 20 December 2012 / *Accepted:* 21 January 2013 / *Published:* 1 February 2013

Based on a strategy for precipitation of a product with lower solubility product constant ($K_{sp}$) by introducing a phase with higher $K_{sp}$, we firstly report a facile microemulsion route through introducing $ZnSO_4$ for synthesizing mesoporous $SnO_2$ submicrospheres at ambient temperature followed by annealing treatment at 873 K for 2 h. As-prepared $SnO_2$ submicrospheres exhibit uniform morphology and high specific surface area. $SnO_2$ nanoparticles achieved here feature high crystallinity, small particle sizes (ca. 4.4 nm) and narrow size distributions, contributing to $SnO_2$ submicrostructures with large reversible capacity (846 $mAh \cdot g^{-1}$ after 50 cycles at a current density of 100 $mA \cdot g^{-1}$) and significantly improved cycling performance. We expect our methodology could act as a reference for preparing a variety of nanoscale materials with novel structure and function in nanotechnology.

**Keywords:** Lithium-ion batteries; Submicrospheres; $SnO_2$; Anode materials

## 1. INTRODUCTION

Recently, many efforts have been made to implant a Sn-based anode into a Li-secondary battery since it was first reported by Idota and co-workers in 1997 [1-4]. With high theoretical reversible lithium storage capacity (782 $mAh \cdot g^{-1}$), more than twice that of the currently commercialized graphite (372 $mAh \cdot g^{-1}$), and low potential of lithium ion intercalation, tin oxide ($SnO_2$) is regard as one of the most promising candidates for anode materials [5-7]. However, similar to other alloy-type anode materials, the main factor limiting the application of $SnO_2$ is the poor cyclic performance due to pulverization and subsequent electrical disconnection of the electrode caused by the extremely large volume change (up to about 300%) during the insertion and extraction processes of $Li^+$ [8-10]. To enhance the cyclability of the electrode, hybridizing $SnO_2$ with carbon is effective, but

this approach sacrifices the capacity itself due to the introduction of carbon and is usually complicated in fabrication [11-14]. It is well established that nanomaterials, especially in hollow or porous nanostructures, hold the key to fundamental advances in shortening path, accommodating large volume change, affording high capacities and rechargeability, owing to the high specific surface area and quantum size effects [15-16].

Consequently, the current strategies mainly address the synthesis of $SnO_2$ nanostructures with different geometrical morphologies, including nanoparticles [17-20], nanorods/belts/wires [2, 21-25], nanodisks [26], nanotubes [27-28], nanoboxes [3, 29], hollow spheres/octahedral [9, 30-32] and hierarchical/mesoporous structures [33-38], by various synthetic approaches such as sol-gel [17-18], solution-phase growth [6, 19-23, 32-36], vapor-phase evaporation [7, 24-26], template-based method [3, 27-28, 31], and molten salt synthesis [21], and so forth.

Since the term "microemulsion" was introduced by Schulman, Stoeckenius and Prince for the first time in the late 1950s [39], microemulsion process (reverse micelle synthesis) has been developed to a powerful route to controlling particle size and size distribution and has been widely used for synthesizing various nanoscale crystallines, such as metallic, metal oxide, semiconductor nanoparticles, and even more complex ceramic nanomaterials [40-43]. A microemulsion is considered as a thermodynamically stable isotropic dispersion of two immiscible liquids since the microdomain of either or both liquids has been stabilized by an interfacial film of surface-active molecules [39-41]. Among all chemical processes, the microemulsion method has proved to be particularly versatile and reproducible superior to many others in terms of delivering homogenous and monodisperse nanoparticles. Therefore, the size, morphology and chemical homogeneity of the resulting nanoparticles can be effectively controlled by proper choice of the composition of the microemulsion system [41-46].

Herein, we report a facile strategy for preparing mesoporous $SnO_2$ submicrospheres via crystalline nanoparticle aggregates by a simple microemulsion route. By introducing $ZnSO_4$, $SnO_2$ precursors will precipitate from microemulsion solutions at room temperature, which is further converted to well-dispersed crystalline nanoparticles (ca. 4.4 nm) after annealing treatment at 873 K for 2 h, leading to high lithium ion storage capacity.

## 2. EXPERIMENTAL

### *2.1 Materials synthesis*

Analytical grade $SnCl_4 \cdot 5H_2O$, $ZnSO_4 \cdot 5H_2O$, *n*-pentanol, cyclohexane and cetyltrimethylammonium bromide (CTAB) were used as received without further purification. Deionized water was used in the experiments. The reaction was carried out in a 50 mL glass cone-shaped bottle at ambient temperature (298 K). In a typical procedure to synthesize $SnO_2$ nanomaterials, two microemulsion solutions were prepared by adding 2.5 mL of 5 mmol $SnCl_4 \cdot 5H_2O$ and 2.5 mL of 10 mmol $ZnSO_4 \cdot 5H_2O$ aqueous solutions to *n*-pentanol/CTAB/cyclohexane systems (*n*-pentanol/CTAB = 18 (mol ratio), $H_2O$/CTAB = 185 (mol ratio), [CTAB] = 0.09 M), respectively,

which were magnetically stirred for 10 min until they became homogeneous and transparent. After that, the two solutions were mixed rapidly, continued to stir for 30 min, and then were set aside at room temperature for 48 h. A white precipitate was harvested after centrifugation, washed with deionized water and absolute ethanol several times, and then dried in an oven at 333 K for 6 h. The precipitates were then transferred to a tube furnace and annealed in air at various temperatures of 673, 773 and 873 K for 2 h to form final products.

### *2.2 Materials characterization*

The synthesized products were characterized by powder X-ray diffraction (XRD, Rigaku-D/Max 2500PC/Japan, using Cu Kα radiation, λ=1.5406 Å), field emission scanning electron microscopy (FESEM, FEIXL-30/USA), transmission electron microscopy (TEM, FEI-TECNAI G2 F20/USA, operating at an accelerating voltage of 200 kV) equipped with energy dispersive X-ray spectroscopy (EDS, EDAX-Genesis/USA). Brunauer-Emmett-Teller (BET) surface area and pore volume were estimated using ASAP 2420 (USA).

### *2.3 Electrochemical measurements*

The annealed products at 873 K for 2 h were mixed with acetylene black (AB) and a binder (poly (vinylidene fluoride), PVDF), in weight ratios of 80:10:10 and 40:40:20, respectively, in a solvent (N-methyl-2-pyrrolidone, NMP). The slurry was uniformly pasted on Cu foil. Such prepared electrode sheets were dried at 393 K for 12 h in a vacuum oven and pressed under a pressure of approximately 4 MPa. The CR2025-type half-coin cells were assembled in an argon-filled glove box with $H_2O$ and $O_2$ contents below 1 ppm. Metallic lithium foil was used as the counter and reference electrode. The electrolyte consists of a solution of 1M $LiPF_6$ in ethylene carbonate (EC), ethyl methyl carbonate (EMC) and dimethyl carbonate (DMC) (with a EC:EMC:DMC volume ratio of 1:1:1). Charge–discharge performances were evaluated by a LAND CT2001A battery instrument at a constant current density within a cutoff window of 0.05-3.0 V at room temperature. Cyclic voltammetry (CV) measurements were carried out on a CHI650D electrochemical workstation over the potential range 0.05-3.0 V vs. $Li/Li^+$ at a scanning rate of 0.1 $mVs^{-1}$.

## 3. RESULTS AND DISCUSSION

Figure 1a-d show XRD for as-synthesized precursors and annealed products at various temperatures (673, 773 and 873 K), respectively. Without annealing treatment, diffraction peaks detected are relatively weak, broad and overlapped (Figure 1a), revealing the presence of imperfect lattice sites and amorphous phases. With the annealing temperature rising from 673 to 773 K, peak intensities increase gradually while the full width at half maximum (FWHM) decrease gently (Figure 1b and c), implying improved crystallinity and expanded particle sizes. As the temperature further

grows to 873 K, the peaks become comparatively sharper (Figure 1d), revealing nanoparticles achieved having better crystallinnity. All peaks can be well indexed as tetragonal rutile-like $SnO_2$ (cassiterite, Joint Committee on Powder Diffraction Standards (JCPDS) card No. 41-1445, space group: $P4_2/nmn$ (136)). No other peaks are detected. Average lattice constants of $SnO_2$ nanoparticles are estimated to be a=b=4.739 and c=3.198 calculated from (110), (101) and (211) diffraction peaks (Figure 1d).

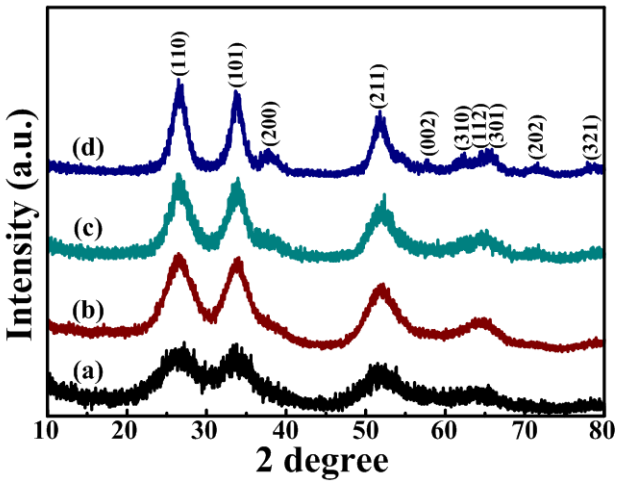


**Figure 1.** XRD patterns of (a) $SnO_2$ precursors and after annealing treatment for 2 h at (b) 673, (c) 773 and (d) 873 K, respectively.

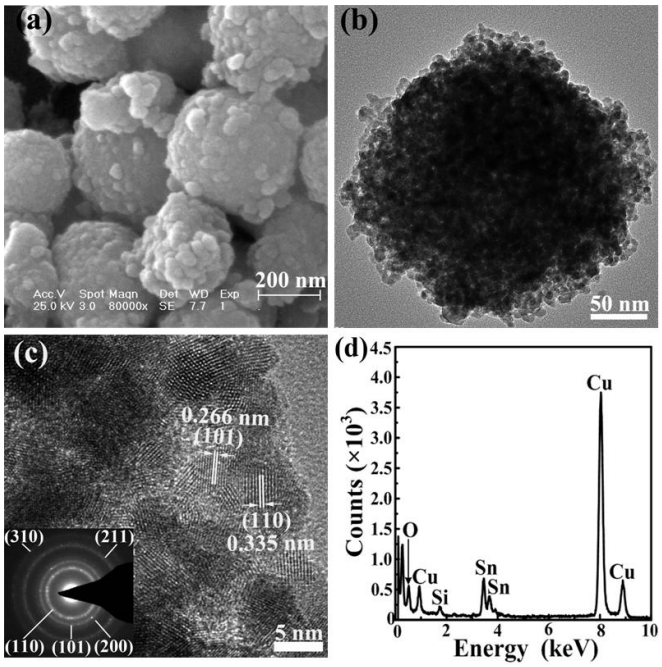


**Figure 2.** Morphological and EDS analyses of $SnO_2$ submicrospheres: (a) FESEM images; (b) TEM images; (c) HRTEM image (SAED pattern is shown in the lower left corner); and (d) EDS analysis.

Figure 2a displays typical FESEM image of annealed products at 873 K for 2h. One can see that products prepared here exhibit coarse surface and spherical morphology with average size of ~350 nm. To explore inherent structures, $SnO_2$ submicrospheres are further characterized by the TEM. Figure 2b clearly show disordered wormhole-like mesoporous pores. The high-resolution TEM image displays $SnO_2$ nanoparticles with ~3.0-5.0 nm size distributions, and lattice fringes of the ones with (110) and (101) planes are frequently observed in Fig. 2c. The selected-area electron diffraction (SAED) pattern (inset in Fig. 2c) indicates that the submicrospheres are polycrystalline, and diffraction rings can be indexed to the (110), (101), (200), (211) and (301) planes, coinciding with the tetragonal $SnO_2$. From typical EDS results (Fig. 2d), the compositions of $SnO_2$ submicrospheres are dominated by O and Sn signals and Cu peaks (derived from the copper foil substrate) accompanying a small Si peak (derived from the EDS probe). No Zn peak is detected under EDS analysis, even though a high concentration of $Zn^{2+}$ (with a designed $Zn^{2+}$:$Sn^{4+}$ molar ratio of 2:1) is introduced into the microemulsion system.

According to XRD and EDS results, we speculate that $SnO_2$ formation reactions in microemulsion systems might be as follows:

$$Sn^{4+}+4OH^{-}\rightarrow Sn(OH)_4\downarrow \quad (1)$$

$$Sn(OH)_4\downarrow\rightarrow SnO_2+2H_2O \quad (2)$$

Note that the $OH^-$ in reaction (1) is produced by the self-ionization reaction of $H_2O$. Since the solubility product constant ($K_{sp}$) for $Sn(OH)_4$ ($1\times10^{-56}$) is much lower than that for $Zn(OH)_2$ ($3\times10^{-17}$) [47], it is not surprising that the precipitation reaction for the former is the dominant reaction when the two microemulsion solutions are mixed together. Moreover, the mixed solutions after precipitation reactions was tested to be acidic (pH=1.0), further confirming that reaction (1) did occur. The acid mixed solution hinders the precipitation reaction of $Zn(OH)_2$ owing to the release of $H^+$ by the self-ionization reaction of $H_2O$. Moreover, the particularly low $OH^-$ concentration in an acidic microemulsion system significantly retards the precipitation and growth of $Sn(OH)_4$ and further makes the growth of $SnO_2$ nanoparticles with small sizes favorable (~3.0-5.0 nm). More importantly, the synthesis process is performed at ambient temperature, which also restricts the growth of precipitates. To the best of our knowledge, this is the lowest temperature reported by far for the synthesis of fine nanoparticles of $SnO_2$.

From TEM images (Fig. 2b and 2c), we can conclude that $SnO_2$ submicrospheres (~350 nm) consists actually of crystalline $SnO_2$ nanoparticle aggregates. It is believed that the impetus for the aggregation of nanoparticles is to eliminate surface energy, which is largely different from classical crystal growth mechanisms of "Ostwald-ripening" [30-31] and "oriented attachment" [48]. It is acknowledged that the crystal growth is generally at the expense of surface area, which impairs the desirable physical and chemical properties of nanoparticles. In this study, however, the aggregates of crystalline $SnO_2$ nanoparticles with wormhole-like mesoporous structure still retain the nature of large specific surface area.

$N_2$ adsorption/desorption isotherms were employed for the products (Fig. 3). One can see that

the samples display a typical IV isotherm curve with a clear adsorption/desorption hysteresis loop, indicating the existence of abundant mesoporous structures in the architectures [49]. The Brunauer-Emmett-Teller (BET) specific surface area are 99.5 $m^2g^{-1}$ for $SnO_2$ submicrospheres. To further analyze the pore structure, pore size distribution curves have been investigated by using Barrett-Joyner-Halenda (BJH) method. The pore size distribution measurement indicates that the $SnO_2$ submicrospheres exhibit a very narrow pore-size distribution with an average pore diameter at ca. 3.6 nm (inset of Fig. 3). The pore size obtained from BJH is consistent with the result from TEM image (Fig. 2c).

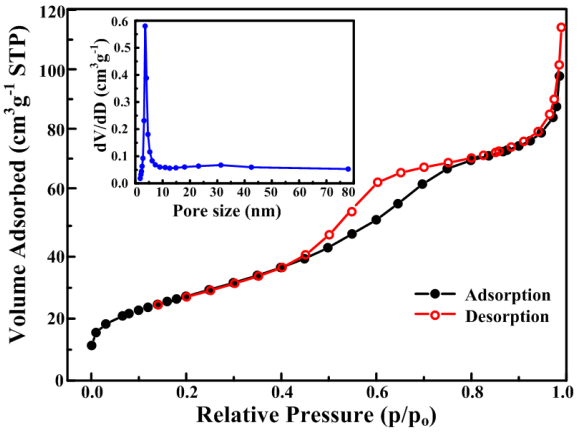


**Figure 3.** Nitrogen adsorption and desorption isotherms of $SnO_2$ submicrospheres with corresponding pore-size distribution (inset) calculated by BJH method from desorption branch.

Motivated by the inherent structure of $SnO_2$ submicrospheres, we have performed lithium storage tests as an anode material with different weight ratios of carbon 10% (sample-1) and 40% (sample-2). Figure 3a and b show initial discharge/charge voltage profiles and cycling performance at a current density of 100 $mA \cdot g^{-1}$ within a cutoff window of 0.05-3.0 V, respectively. The initial discharge and charge capacities are 1733 and 960 $mAh \cdot g^{-1}$, and 2801 and 1566 $mAh \cdot g^{-1}$ for sample-1 and sample-2, respectively. The large capacity loss in the first cycle for both samples is mainly attributed to the initial irreversible formation of $Li_2O$, and other irreversible processes such as trapping of some lithium in the lattice, inevitable formation of solid electrolyte interface (SEI layer) and electrolyte decomposition, which are common for most anode materials [28, 30]. Moreover, it is clearly that the first discharge and charge capacities of the sample-2 are significantly higher than those of sample-1. More importantly, the sample-2 exhibits a much better cycling performance than sample-1 (Fig. 4b). For the sample-1, the reversible capacity rapidly decreased with the increasing cycle numbers. The capacity was only 203 $mAh \cdot g^{-1}$ after 30 cycles, which is below capacity of pure carbon (302 $mAh \cdot g^{-1}$). In contrast, the reversible capacity of the sample-2 retains 846 $mA \cdot g^{-1}$ after 50 cycles. This improvement of cyclability indicated that the conductive carbon content affect the $SnO_2$ submicrospheres performance as anode material for lithium ion batteries. Similar phenomenon has been observed in previous literature [50].

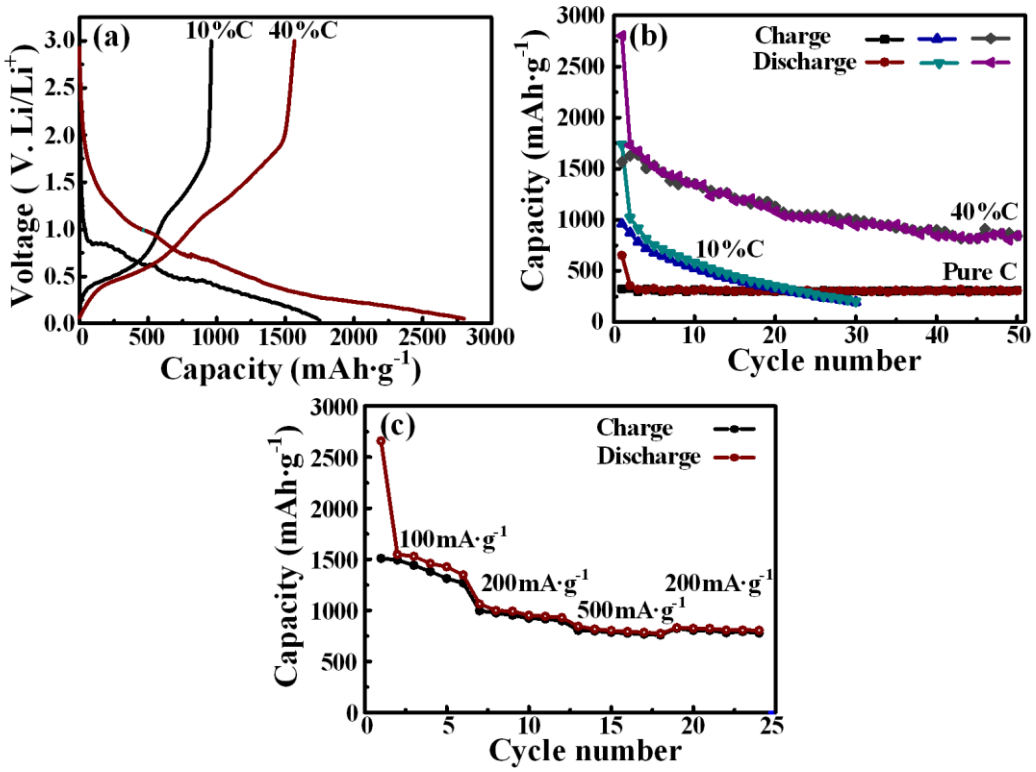


**Figure 4.** Electrochemical performance of $SnO_2$ submicrospheres: (a) discharge/charge profiles; (b) cycling performance; and (c) cycling properties with various current densities.

In addition, the sample-2 exhibits better rate capability at various current densities of 100, 200 and 500 $mA \cdot g^{-1}$ (Fig. 4c). The discharge capacity at the 100 $mA \cdot g^{-1}$ is 1347 $mAh \cdot g^{-1}$ over 6 cycles, and the capacity at the 200 $mA \cdot g^{-1}$ is 929 $mAh \cdot g^{-1}$ over 12 cycles. Even at a high current density of 500 $mA \cdot g^{-1}$, it retains high capacity of 774 $mAh \cdot g^{-1}$ over 18 cycles. After the current density bounces to 200 $mA \cdot g^{-1}$, the electrode delivers a capacity of about 805 $mAh \cdot g^{-1}$ over 24 cycles.

## 4. CONCLUSION

In summary, mesoporous $SnO_2$ submicrospheres via crystalline nanoparticle aggregates with uniform morphology can be facilely synthesized by microemulsion method at ambient temperature followed by annealing treatment at 873 K for 2 h. The $SnO_2$ nanoparticles achieved here feature high crystallinity, small particle sizes and narrow size distributions. As an anode material in lithium-ion batteries, $SnO_2$ submicrospheres exhibit a particularly large reversible capacity (846 $mAh \cdot g^{-1}$ after 50 cycles) and significantly enhanced cycling performance. A synthesis strategy for precipitation of a product with lower $K_{sp}$ by introducing a phase with higher $K_{sp}$ can also be developed for the preparation of other nanoscale products during microemulsion synthesis.

ACKNOWLEDGEMENT
This work is supported by Foundation of Jilin University for Distinguished Young Scholars and Project 985-High Performance Materials and Advanced Manufacturing Technology of Jilin University.

**References**

1. Y.M. Chiang, *Science* 330 (2010) 1485-1486.
2. J.Y. Huang, L. Zhong, C.M. Wang, J.P. Sullivan, W. Xu, L.Q. Zhang, S.X. Mao, N.S. Hudak, X.H. Liu, A. Subramanian, H. Fan, L. Qi, A. Kushima, J. Li, *Science* 330 (2010) 1515-1520.
3. Z. Wang, D. Luan, F.Y.C. Boey, X.W. Lou, *J. Am. Chem. Soc*. 133 (2011) 4738-4741.
4. L. Cai, J. Shen, F. Cheng, Z. Tao, J. Chen, *J. Power Soures* 196 (2011) 2195-2201.
5. C. Wang, Y. Zhou, M. Ge, X. Xu, Z. Zhang, J.Z. Jiang, *J. Am. Chem. Soc*. 132 (2010) 46-47.
6. C. Kim, M. Noh, M. Choi, J. Cho, B. Park, *Chem. Mater*. 17 (2005) 3297-3301.
7. M.S. Park, G.X. Wang, Y.M. Kang, D. Wexler, S.X. Dou, H.K. Liu, *Angew. Chem. Int. Ed.* 46 (2007) 750-753.
8. J.M. Tarascon, M. Armand, *Nature* 414 (2001) 359-367.
9. S. Ding, X.W. Lou, *Nanoscale*. 3 (2011) 3586-3588.
10. S. Nam, S. Kim, S. Wi, H. Choi, S. Byun, S.M. Choi, S.I. Yoo, K.T. Lee, B. Park, *J. Power Sources* 211 (2012) 154-160.
11. S.M. Paek, E.J. Yoo, L. Honma, *Nano Lett.* 9 (2009) 72-75.
12. X.W. Lou, C.M. Li, L.A. Archer, *Adv. Mater.* 21 (2009) 2536-2539.
13. D. Ahn, X. Xiao, Y. Li, A.K. Sachdev, H.W. Park, A. Yu, Z. Chen, *J. Power Sources* 212 (2012) 66-72.
14. Z. Wen, Q. Wang, Q. Zhang, J. Li, *Adv. Funct. Mater*. 17 (2007) 2772-2778.
15. M. Armand, J.M. Tarascon, *Nature* 451 (2008) 652-657.
16. A.S. Aricò, P. Bruce, B. Scrosati, J.M. Tarascon, W. Schalkwijk, *Nature Mater.* 4 (2005) 366-377.
17. N.L. Wu, S.Y. Wang, A. Rusakova, *Science* 285 (1999) 1375-1377.
18. M.S. Park, Y.M. Kang, G.X. Wang, S.X. Dou, H.K. Liu, *Adv. Funct. Mater*. 18 (2008) 455-461.
19. G. Pang, S. Chen, Y. Koltypin, A. Zaban, S. Feng, A. Gedanken, *Nano Lett*. 1 (2001) 723-726.
20. X. Wang, J. Zhuang, Q. Peng, Y. Li, *Nature* 437 (2005) 121-124.
21. Y. Liu, C. Zheng, W. Wang, C. Yin, G. Wang, *Adv. Mater.* 13 (2001) 1883-1886.
22. B. Cheng, J.M. Russell, W. Shi, L. Zhang, E.T. Samulski, *J. Am. Chem. Soc*. 126 (2004) 5972-5973.
23. L. Vayssieres, M. Graetzel, *Angew. Chem. Int. Ed*. 43 (2004) 3666-3670.
24. Z.W. Pan, Z.R. Dai, Z.L. Wang, *Science* 291 (2001) 1947-1949.
25. H.T. Chen, S.J. Xiong, X.L. Wu, J. Zhu, J.C. Shen, P.K. Chu, *Nano Lett*. 9 (2009) 1926-1931.
26. Z.R. Dai, Z.W. Pan, Z.L. Wang, *J. Am. Chem. Soc*. 124 (2002) 8673-8680.
27. L. Zhao, M. Yosef, M. Steinhart, P. Goring, H. Hofmeister, U. Gosele, S. Schlecht, *Angew. Chem. Int. Ed*. 45 (2006) 311-315.
28. J. Ye, H. Zhang, R. Yang, X. Li, L. Qi, *Small.* 6 (2010) 296-306.
29. Y. Liu, J. Dong, M. Liu, *Adv. Mater*. 16 (2004) 353-356.
30. X.W. Lou, Y. Wang, C. Yuan, J.Y. Lee, L.A. Archer, *Adv. Mater*. 18 (2006) 2325-2329.
31. X.W. Lou, L.A. Archer, Z. Yang, *Adv. Mater.* 20 (2008) 3987-4019.
32. J.S. Chen, C.M. Li, W.W. Zhou, Q.Y. Yan, L.A. Archer, X.W. Lou, *Nanoscale*. 1 (2009) 280-285.
33. M. Fang, X. Tan, B. Cheng, L. Zhang, *J. Mater. Chem*. 19 (2009) 1320-1324.
34. L.Y. Jiang, X.L. Wu, Y.G. Guo, L.J. Wan, *J. Phys. Chem. C* 113 (2009) 14213-14219.
35. H. Wang, Q. Liang, W. Wang, Y. An, J. Li, L. Guo, *Cryst. Growth Des*. 11 (2011) 2942-1947.
36. R.D. Cakan, Y.S. Hu, M. Antonietti, J. Maier, M.M. Titirici, *Chem. Mater*. 20 (2008) 1227-1229.
37. Z. Wen, G. Wang, W. Lu, Q. Wang, Q. Zhang, J. Li, *Cryst. Growth Des*. 7 (2007) 1722-1725.

38. X. Yin, L. Chen, C. Li, Q. Hao, S. Liu, Q. Li, E. Zhang, T. Wang, *Electrochim Acta* 56 (2011) 2358-2363.
39. J.H. Schulman, W. Stoeckenius, L.M. Prince, J. Phys. Chem. 63 (1959) 1677-1680.
40. M. J. Schwuger, K. Stickdornt, *Chem. Rev*. 95 (1995) 849-864.
41. H. Groger, F. Gyger, P. Leidinger, C. Zurmuhl, C. Feldmann, *Adv. Mater*. 21 (2009) 1586-1590.
42. A.K. Ganguli, T. Ahmad, S. Vaidya, J. Ahmed, *Pure Appl. Chem.* 80 (2008) 2451-2477.
43. V. Juttukonda, R.L. Paddock, J.E. Raymond, D. Denomme, A.E. Richardson, L.E. Slusher, B.D. Fahlman, *J. Am. Chem. Soc*. 128 (2006) 420-421.
44. J.X. Zhou, M.S. Zhang, J.M. Hong, J.L. Fang, Z. Yin, *Appl. Phys. A*. 81 (2005) 177-182.
45. D. Chen, L. Gao, *J. Colloid Interface Sci*. 279 (2004) 137-142.
46. D.F. Zhang, L.D. Sun, J.L. Yin, C.H.Yan, *Adv. Mater*. 15 (2003) 1022-1025.
47. J.G. Speight, Lange's handbook of chemistry, 16 th, ed. MCGRAW-HILL Inc. New York, 2004, ISSN 0748-4585.
48. R.L. Penn, J.F. Banfield, *Science* 281 (1998) 969-971.
49. L. Shen, C. Yuan, H. Luo, X. Zhang, L. Chen, H. Li, *J. Mater. Chem.* 21 (2011) 14414-14416.
50. H. Liu, G. Wang, J. Park, J. Wang, H. Liu, C. Zhang, *Electrochim. Acta*. 54 (2009) 1733-1736.